


Cite this: *RSC Adv.*, 2022, 12, 30871

Multiband-switchability and high-absorptivity of a metamaterial perfect absorber based on a plasmonic resonant structure in the near-infrared region

Jian Liang, Yan Chen,^{ID}* Zhangkun Zhou and Shanjun Chen*

Metamaterials are widely studied in bio-photonics because of their flexible and tunable resonance wavelengths in the near-infrared region and their particular relevance to biological tissues. In this paper, we propose for the first time a perfect absorber that is switchable between triple-band and dual-band absorption. The narrowband metamaterial perfect absorber has a conventional metal–dielectric–metal structure, which consists of an array of silver disks, a silica dielectric layer and a gold substrate. Its working performance is mainly determined by the height, radius and period of the top silver disks. By adjusting these parameters, the perfect absorber can be switched between triple-band and dual-band absorption with the peaks showing close to 100% absorbance. This makes it possible to use it as a multifunctional absorber in various applications, such as filters and sensors.

Received 6th September 2022

Accepted 11th October 2022

DOI: 10.1039/d2ra05617h

rsc.li/rsc-advances

1. Introduction

Metamaterials are artificial materials with properties that are dependent on their subwavelength structure, rather than on their chemical composition, and they have some unique properties not found in naturally occurring materials.^{1–3} Increasing attention has been paid to perfect absorbers (PA) that are based on metamaterials. The study of metamaterial absorbers shows that the surface plasmons (SPs) in metal micro/nano-structures play an important role in the metamaterial perfect absorber (MPA) due to their strong field confinement and enhancement.⁴ SPs can be classified as propagating surface plasmons (PSPs) and local surface plasmons (LSPs).^{5–8} PSPs are mainly associated with periodic structures, while LSPs are mainly associated with metal particles whose structural dimensions are much smaller than the wavelength of incident waves.

Metamaterial absorbers (MAs) typically consist of three layers in a metal–dielectric–metal (MDM) structure, *i.e.*, the patterned metal antenna and the thick metal mirror layers are separated by a thin dielectric spacer.^{9–15} The MDM structure is ideal for designing an MPA, for this kind of structure of MPA can store the internal electromagnetic energy and then dissipate it gradually. The unitary structure of the MDM absorber, also known as a meta-atom, primarily has a regular and simple geometry, including squares,¹⁶ rectangles,¹⁷ crosses¹⁸ and circles.¹⁹ So far, the studies on these absorbers have extended to various wavelength bands, such as microwave,^{20,21} terahertz,^{22–25}

long-wave infrared,²⁶ mid-wave infrared²⁷ and visible–near-infrared bands.²⁸ It is worth mentioning that Karmakar *et al.*²⁵ designed a metamaterial refractive index sensor by making use of the tuning effect of Fano resonance in the THz band in a geometrically symmetric stacked metamaterial. Its features, such as being multifunctional, highly compact, miniaturized and well-integrated make it promising for commercial use in the future. MPAs are also widely studied for their wide range of potential applications, such as energy harvesting,²⁹ thermal emitters,³⁰ detectors,³¹ and sensors.^{32,33} Singh *et al.*³³ designed and constructed a novel spanner resonator for the detection of refractive index changes in biological samples. It could also be used to detect other components, such as human blood type, and ethanol and hemoglobin concentrations. In recent years, various structures, including composites consisting of different simple superatomic and multilayer structures, have been proposed to achieve multiband absorption. Hong *et al.*³⁴ achieved narrow-band absorption using only a silver substrate and silicon particles. However, due to the simple structure and the few adjustable parameters, the performance of the absorber was not very satisfactory. A multifunctional absorber has been designed by Zhang *et al.*³⁵ The absorber can achieve broadband and narrowband absorption from positive and negative angles of incidence, respectively. However, the design mentioned above will complicate the fabrication and limit the size of the device and its efficiency. This makes industrial manufacturing much more costly and is not conducive to the same level of mass manufacturing. Moreover, most narrowband MPAs have only a single function and are not adjustable for the number of absorption peaks, which greatly limits the use of absorbers.

School of Physics and Optoelectronic Engineering, Yangtze University, Jingzhou, 434023, P. R. China. E-mail: chenyan@yangtzeu.edu.cn; csj@yangtzeu.edu.cn



Therefore, a perfect absorber with a simple and versatile structure needs to be invented.

In this paper, we propose a simple MDM structure that can achieve high absorption. In addition, we analyze three different modes by combining electric field intensity images with absorption spectra recorded when varying the structural parameters. To our knowledge, we obtain, for the first time, a switch between triple-band and dual-band absorption peaks in the near-infrared region by adjusting the structural parameters, and a near 100% absorbance for the two peaks as well. This provides a new route to infrared biomolecular detection.

2. Modes and methods

The MDM structural unit of the metamaterial is shown in Fig. 1(a). The finite-difference time-domain (FDTD) method is used to simulate the absorber we designed. The metamaterial absorber structure consists of three layers, as shown in Fig. 1(b). In the proposed MDM structure, the dielectric layer SiO_2 is sandwiched in between the top silver array and the bottom gold film. The use of SiO_2 will reduce the propagation loss significantly, thereby increasing the propagation length of the surface plasmons. In the visible to near-infrared (NIR) region, silver is placed on the top layer of the structure as an active layer due to its low inherent loss characteristics. The bottom gold film serves as the substrate mainly to prevent the transmission of incident light. The light is incident perpendicularly along the negative direction of the z -axis. The thickness of the Au is larger than the depth of the penetration of electromagnetic waves in the infrared region to ensure the near-zero transmission of incident light. A thin silica dielectric layer separates the two metal layers as an isolator. The radius and the height of the nanodisks are expressed as r and h , respectively, and the period of the array is designated as p . The thickness of the dielectric layer is denoted by d . The permittivity of the Ag, SiO_2 and Au layers is as described by Palik.³⁶ Periodic boundary conditions are used in the x - and y -directions, while, in the z -direction, a perfectly matched layers (PML) boundary condition is adopted. The plane wave is incident vertically from the top. In the experiment, the fabrication process is shown in Fig. 2 and the process is as follows: the SiO_2 is deposited onto a gold substrate using the conventional electron beam evaporation method.³⁷ A mask (shown in

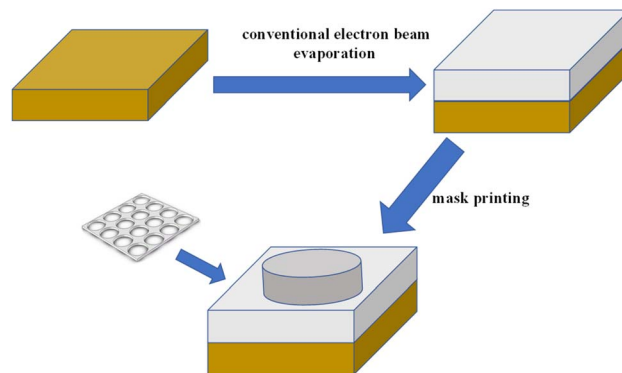


Fig. 2 Schematic illustration of the fabrication process for the absorber.

Fig. 2) is placed close to the dielectric layer to form the top Ag disk by using e-beam deposition. Since the structure we designed is simple, we only need to design masks of different structure sizes to realize the adjustment of the parameters of the structure. This scheme can be used in the dual-band and triple-band switching mentioned later.

3. Results and analysis

The absorption can be calculated from $A = 1 - R - T$, where R and T are the reflection and transmission, respectively. When the thickness of the metal plane is larger than the depth of its skin in the near-infrared (NIR) range, the transmission of the proposed structure is almost zero and the absorption is only related to the reflection (R)³⁸. Therefore, $A = 1 - R - T \approx 1 - R$. The absorption spectrum of the proposed MDM structure is shown in Fig. 3. We denote the three absorption peaks in order of increasing wavelength as mode 1, mode 2 and mode 3, respectively. At $\lambda_1 = 783$ nm, the absorbance is 99.5%. The full width at half maximum (FWHM) is about 12 nm. Two other absorption bands appear at $\lambda_2 = 977$ nm and $\lambda_3 = 1166$ nm with absorbance values as high as 88.9% and 99.4%, respectively. The results of our parameter optimization are shown in Fig. 4.

In the case of a plane wave incident perpendicularly, the position of the PSP mode in the periodic structure can be obtained using the following formula:^{39,40}

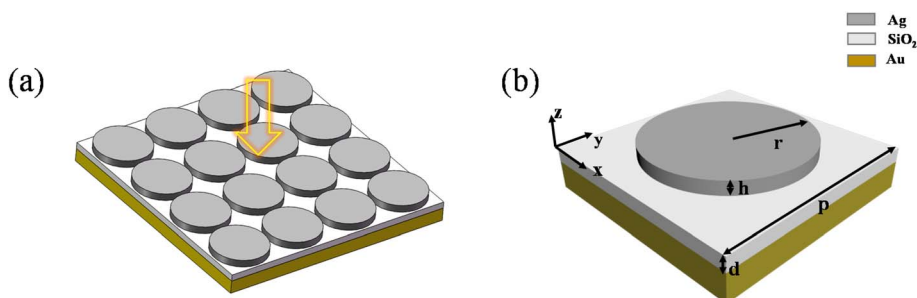


Fig. 1 (a) Three-dimensional schematic diagram of the MDM periodic perfect absorber (16 units). (b) Schematic of a single unit of the metamaterial absorber (MA).



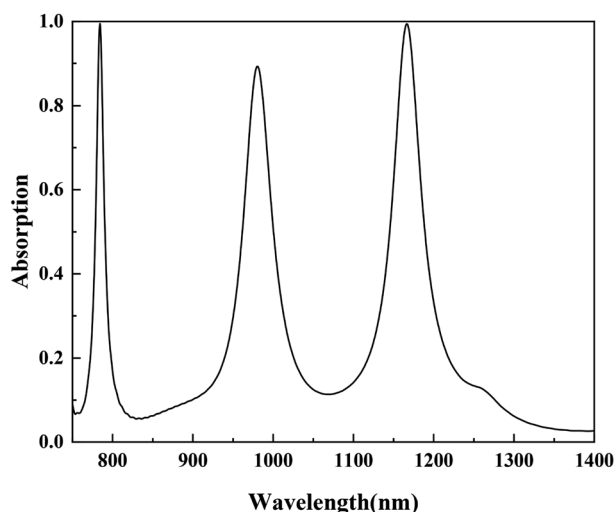


Fig. 3 Absorption spectra of triple-band absorption. The radius and height of the silver particles are $r = 345$ nm and $h = 80$ nm, respectively. The height of the intermediate medium is $d = 85$ nm.

$$\lambda_{\text{PSP}} = \frac{p}{\sqrt{i^2 + j^2}} \left(\frac{\varepsilon_1 \varepsilon_2}{\varepsilon_1 + \varepsilon_2} \right)^{1/2} \quad (1)$$

where p is the period of the array structure, (i, j) is the resonance order, and ε_1 and ε_2 are the dielectric constants of the environment and the metal, respectively. According to the above expression, for an array structure with a period $p = 750$ nm, the resonance wavelength of its PSP mode is approximately 780 nm. A gap resonance mode caused by the SPs will appear here, because, if the metal particles are close to each other or to the metal substrate, the free electrons and the electromagnetic field on both sides of the gap will produce a resonance effect. Thus, the gap mode is formed. The simplest way for gap resonance mode formation to occur is to place a cylindrical nanowire⁴¹ or nanosphere particles⁴² directly on the substrate. Strong electromagnetic coupling occurs between the metal and the substrate. In our proposed structure, both the gap between adjacent Ag particles, and the gap between the Ag particles and the bottom Au layer can be used as conditions for the formation of the gap resonance mode. From Fig. 4, and referring to eqn (1), we can see that mode 1 is the result of the coupling of the PSPs with the gap mode. And the gap pattern is mainly due to the interaction of adjacent particles. When h and d happen to change, mode 1 remains essentially unchanged, as demonstrated from Fig. 4(a and b). We can also see from Fig. 4(c) that an increase in the top layer radius r will lead to the absorption peak of mode 1 to be red-shifted, and, at the same time, the absorption will increase at first and then decrease. As seen from the periodic scan results shown in Fig. 4(d), when p changes from $p = 700$ nm to $p = 725$ nm, there is a sudden change in both mode 1 and mode 3. It can be seen that the absorption peak of mode 1 is first blue-shifted and then red-shifted. When the particle gap is small, the gap mode plays a dominant role. When an increase in particle spacing occurs gradually, PSPs have a greater impact on the blue-shifting of the absorption

peak than the gap mode does.⁴³ When $p = 825$ nm, the role of the propagating surface plasmons is weakened, and the absorption peak almost disappears.

The formation of mode 2 is the result of coupling between the PSPs and LSPs, but is mainly due to the LSPs. A more pronounced blue-shift with an increase in d is illustrated in Fig. 4(a), but the absorption rate does not change any more. This is because the change in dielectric layer thickness can only change the phase of light in the dielectric layer,⁴⁴ so the effect on the absorption rate is not significant. Fig. 4(c) shows that when the radius of the top layer increases, the absorption peak is red-shifted and the absorbance increases. When the period increases, the absorption peak is red-shifted and the absorbance decreases. This is mainly due to the fact that this mode is formed by the coupling of the PSPs and LSPs. Increasing the top radius and decreasing the period will cause an increase in the particle spacing and an increase in propagating surface plasmons. As a result, it will lead to an increase in the absorption rate.

For mode 3, the gap mode plays a major role. Unlike mode 1, the gap mode here is mainly the result of the interaction between the particles and the gold film. As we can see from Fig. 4(a and b), changing d has a notable effect on the phase of the absorption peak. The change in d also causes a blue-shift of the absorption peak, but has little effect on the absorption rate. On the other hand, however, changing h has little effect on either. We can see from Fig. 4(c) that the absorption peak of mode 3 is red-shifted, and the absorption increases first and then decreases. This is consistent with the results of varying p shown in Fig. 4(d). Increasing p leads to a blue-shift of the absorption peak, and then causes the absorption rate to decrease when p reaches 750 nm, indicating that the interparticle interaction becomes weak and leads to the gradual weakening of the gap mode.⁴⁵ Both larger r and smaller p will decrease the amount of light entering the gap. Therefore, too large a radius or too small a period will cause the gap pattern to disappear.

In order to validate the previous analysis of the three modes further, we present Fig. 5 in which the electric and magnetic field intensities are normalized. In the previous section, we determined that mode 1 is the result of the coupling of the PSPs with the gap mode. So, it can be seen that the electric field is distributed in the particle gap, as shown in Fig. 5(a and d). In terms of magnetic field distribution, the gap mode is mainly generated by the gap between silver particles, which confirms the previous statement. It can also be seen in Fig. 5(b and e) that the electric and magnetic fields are localized in the dielectric layer between the silver particles and the gold substrate. This suggests that the main cause of the generation of mode 2 is due to LSPs. Fig. 5(c and f) show that the electric field is distributed in the silver particle gap, while the magnetic field is distributed in the gap that is formed between adjacent silver particles and the gold film. This indicates that the gap pattern of mode 3 is generated by the silver particles and the gold film. The results of the three modes are consistent with those of the previous analysis.



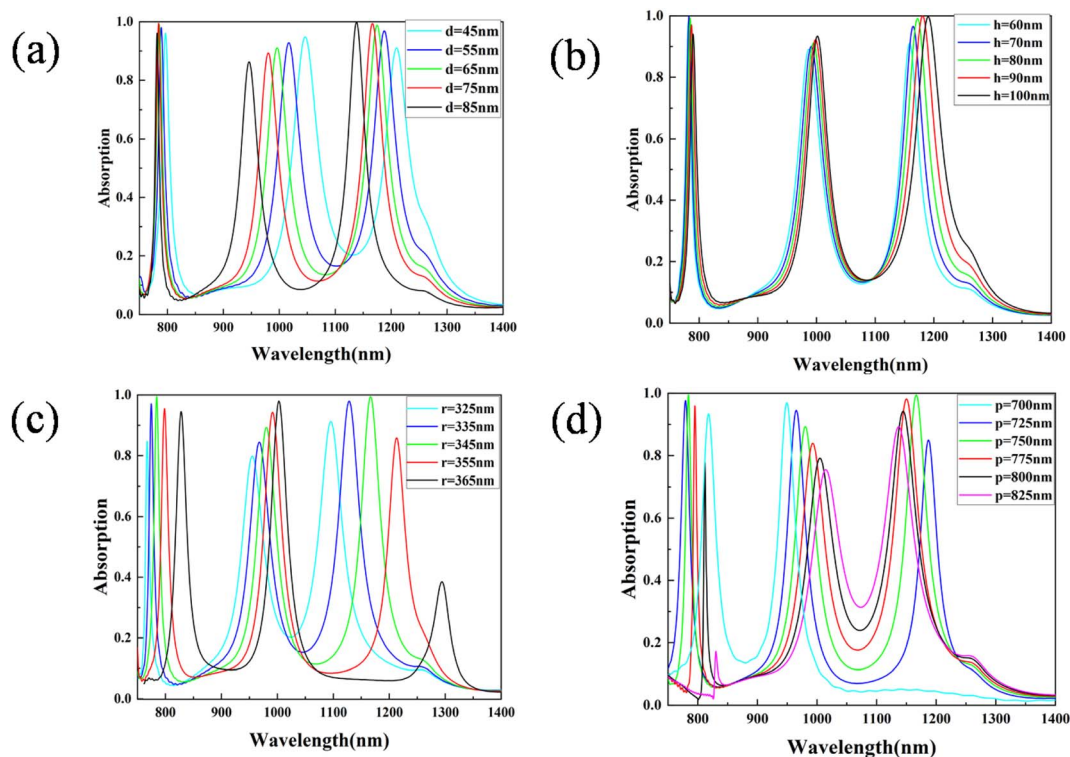


Fig. 4 The relationship between dielectric thickness d (a), the thickness h and the radius r of the silver particles (b) and (c), the period p of the silver array (d) and the absorption rate. Parameters: (a) $r = 345$ nm, $p = 750$ nm, $h = 85$ nm. (b) $d = 80$ nm, $r = 345$ nm, $p = 750$ nm. (c) $h = 85$ nm, $d = 85$ nm, $p = 750$ nm. (d) $h = 85$ nm, $d = 80$ nm, $r = 345$ nm.

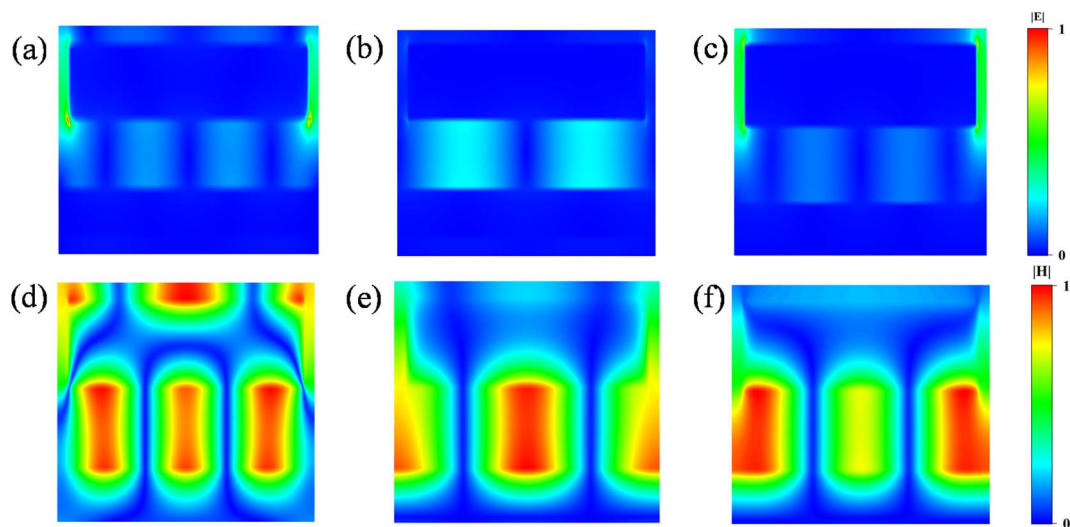


Fig. 5 Normalized electric field (a)–(c) and magnetic field (d)–(f) intensity distributions of the mode 1, mode 2, and mode 3 light absorption bands at the xOz -plane, respectively.

From Fig. 4(d), when p changes from $p = 700$ nm to $p = 725$ nm, there is a sudden change in both mode 1 and mode 3. To understand the exact cause of this pattern, a finer parametric scan is performed in the range of p between $p = 700$ nm and $p = 725$ nm in Fig. 6(a). For mode 1, $p = 700$ nm to 725 nm, the gap mode plays a major role. This results in a blue-shift of the

absorption peak. From Fig. 4(d), when $p = 725$ nm, the PSP mode plays a major role, and then the absorption peak starts to red-shift as the period increases. This result is consistent with the previous analysis. For mode 3, the gap pattern is generated with a large variation in absorption rate. The blue-shift of the absorption peak with increasing period is consistent with



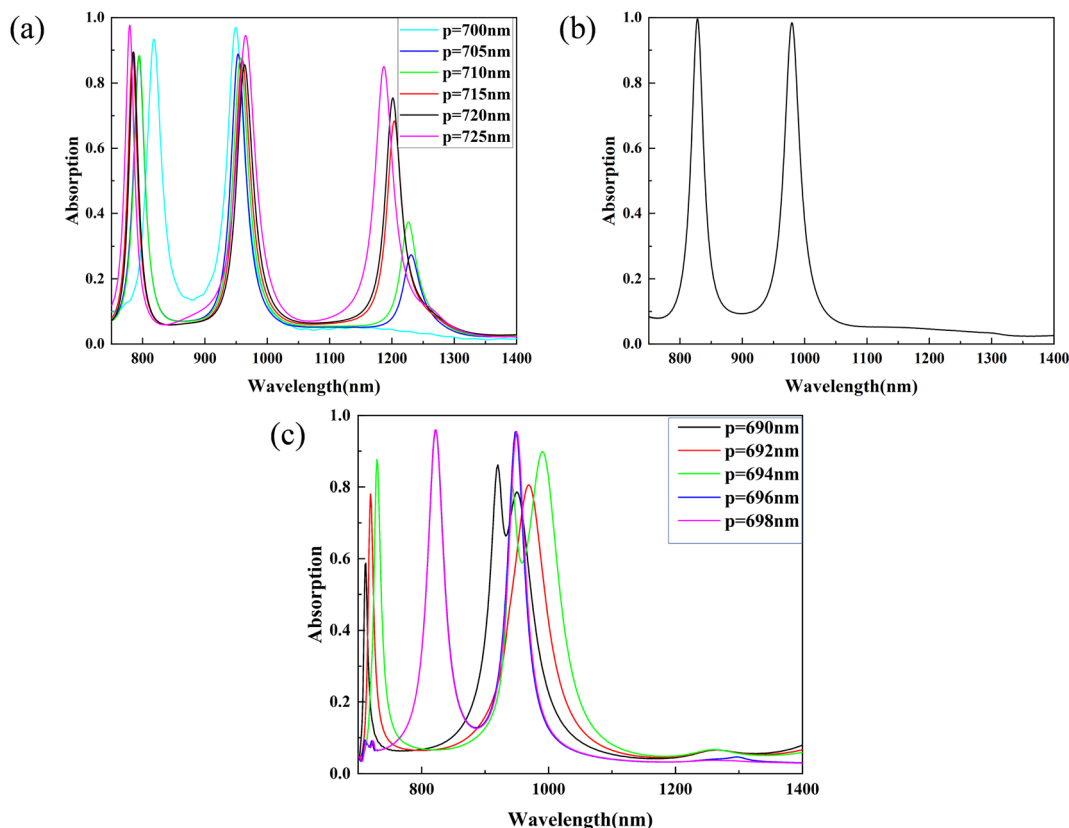


Fig. 6 (a) The relationship between the period (from 700 nm to 720 nm) and the absorption peaks. (b) A spectrum of dual-band absorption. (c) The relationship between the period (from 690 nm to 698 nm) and the absorption peaks.

previous findings. When $p = 700$ nm, only two absorption peaks are left. Adjusting to $h = 40$ nm and $d = 60$ nm can achieve a dual-band perfect absorber. The absorbance of the two peaks reaches 99.6% and 98.4% for modes 1 and 2, respectively, as shown in Fig. 6(b). In Fig. 3 and 6(b), under specific structural parameters, the best absorption performance is achieved for the triple-band and dual-band absorption, respectively. We can switch between dual-band and triple-band filters simply by adjusting the structural parameters. Fig. 6(c) then shows the

effect of reducing the structural period p . As p changes from 696 nm to 694 nm, the absorbance of absorption peak 1 drops sharply, and splitting of absorption peak 2 occurs. This is because of near-field interactions that disrupt the resonance mode and affect the absorption performance of the absorber when the silver particles are too close to each other.⁴⁶

Next, we evaluate two important metrics in sensor applications, namely refractive index sensitivity (S) and figure of merit (FOM) values. S is defined as the ratio of the shift of the

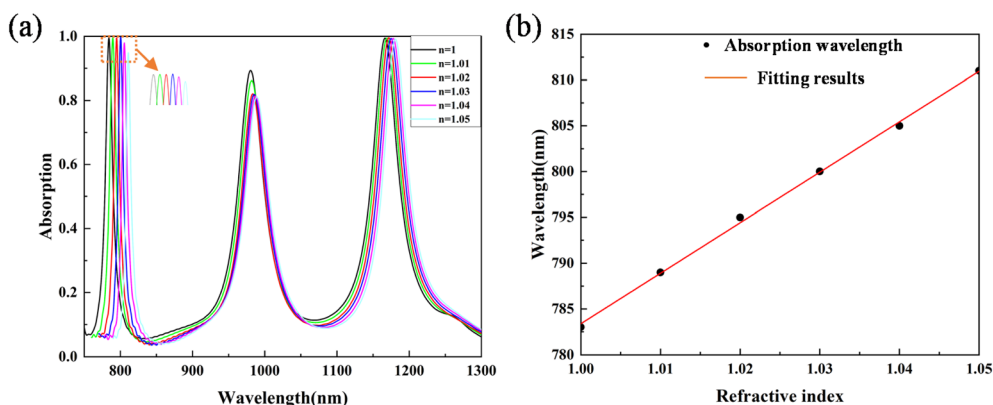


Fig. 7 (a) The relationship between the refractive index and the absorption peaks. (b) The relationship between the wavelength of the absorption peak (mode 1) and the refractive index.

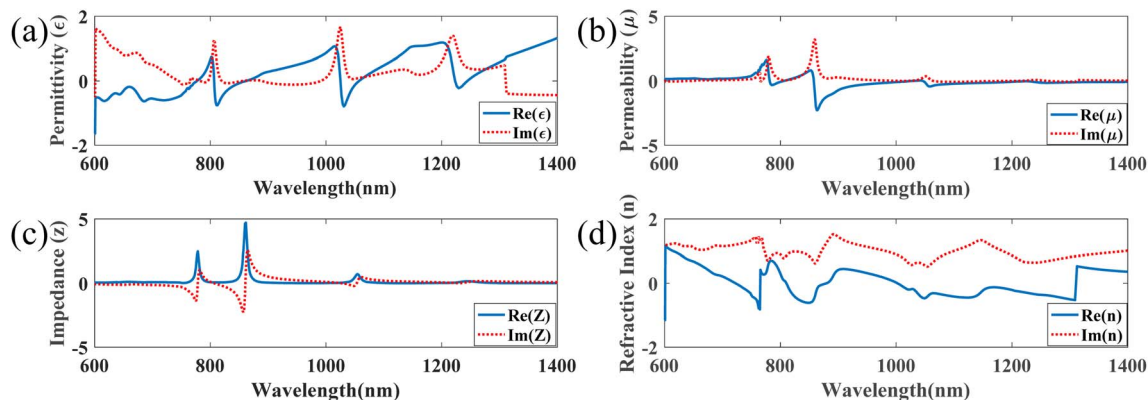


Fig. 8 The simulation results for the metamaterial of permittivity (a), permeability (b), impedance (c) and refractive index (d).

resonance peak ($\Delta\lambda$) to the change in refractive index (Δn), *i.e.*, $S = \Delta\lambda/\Delta n$. The FOM is expressed as the ratio of S to the full width at half maximum (FWHM) of the resonant mode, *i.e.*, $FOM = S/FWHM$. Fig. 7(a) demonstrates the effect of changing the refractive index from 1 to 1.05 on the absorption spectrum. It is shown that the results of mode 1 with low variations in absorbance and minimal FWHM values are relatively better than the results for the other two modes. Fig. 7(b) shows the mode 1 absorption peak wavelength *versus* refractive index, where a good linear approximation exists. By calculating the slope of the fitted straight line, a sensitivity of 551 nm per refractive index unit (RIU) is determined. The value of the FWHM is 12 nm, and the calculated value of the FOM is 46. It is important that a versatile perfect absorber can switch between different numbers of absorption peaks to have a good sensing performance.

Finally, in order to understand the inner physical mechanism of the perfect absorption, we give the simulation results of the equivalent electromagnetic parameters for the metamaterial, as shown in Fig. 8. Fig. 8(a–d) show the permittivity, permeability, impedance and refractive index, respectively, as functions of the wavelength. From the impedance matching theory, surface plasmons are generated when the absorber matches the impedance of free space ($Z = Z_0$).⁴⁷ That is to say, as the impedance of the real part is close to 1 and the imaginary part is close to 0, the higher the absorption of the structure will be. The results of Fig. 8(c) are basically the same as the absorption curve. Therefore, this explains the physical mechanism of perfect absorption theoretically.

4. Conclusions

In this study, we have proposed a metamaterial perfect absorber with a simple structure and a high absorption rate, which allows for dual- and triple-band switching. The absorber is composed of three layers of metal–dielectric–metal. The simple structure makes it conducive to industrial manufacturing. By combining electric field images with absorption spectra recorded when varying the structural parameters, we have analyzed the patterns of the three absorption peaks. By adjusting the

parameters, dual-band and triple-band switching can be realized, and the absorbance of two peaks can approach 100%. We have proposed a new direction and an idea for a multifunctional perfect absorber. The multifunctional absorber can be used for filters, biosensing or other photonic devices.

Author contributions

Jian Liang: investigation, methodology, software, validation, formal analysis, writing – original draft, writing – review & editing. Yan Chen: investigation, methodology, software, validation, formal analysis, conceptualization, supervision, writing – review & editing. Zhangkun Zhou: formal analysis, data curation, writing – review & editing. Shanjun Chen: conceptualization, supervision, writing – review & editing, funding acquisition.

Conflicts of interest

The authors declare that they have no known competing financial interests or personal relationships that could have appeared to influence the work reported in this paper.

Acknowledgements

This work was supported by the National Natural Science Foundation of China (No. 91961107). The authors would like to thank Prof. Liping Fu and doctoral candidate Jingyu Wang for some help during the preparation of this paper.

References

- 1 D. Schurig, J. J. Mock, B. J. Justice, S. A. Cummer, J. B. Pendry, A. F. Starr and D. R. Smith, Metamaterial electromagnetic cloak at microwave frequencies, *Science*, 2006, **314**, 977–980.
- 2 H. T. Chen, H. T. Chen, W. J. Padilla, W. J. Padilla, J. M. O. Zide, J. M. O. Zide, A. C. Gossard, A. C. Gossard, A. J. Taylor, A. J. Taylor, R. D. Averitt and R. D. Averitt, Active terahertz metamaterial devices, *Nature*, 2006, **444**, 597–600.



- 3 R. Sharma and H. Singh, Left handed material antenna design for gsm 1.8 GHz applications, *Proceedings of 2015 RAECS UIET Panjab University Chandigarh 21-22nd December*, 2015.
- 4 Y. Chen, S. Chen, T. M. Shih, J. Y. Wang, W. Y. Li, H. Qian and Z. L. Yang, Broadband unidirectional scattering in visible ranges and controllable hot-spot spatial transfer via a single nanoparticle, *Appl. Surf. Sci.*, 2020, **528**, 146489.
- 5 Y. Jung, I. H. wang, J. Yu, J. Lee, J. H. Choi, J. H. Jeong, J. Y. Jung and J. Lee, Fano metamaterials on nanopedestals for plasmon-enhanced infrared spectroscopy, *Sci. Rep.*, 2019, **9**, 7834.
- 6 A. V. Zayats and I. I. Smolyaninov, Near-field photonics: surface plasmon polaritons and localized surface plasmons, *J. Opt. A: Pure Appl. Opt.*, 2003, **5**, S16–S50.
- 7 H. Raether, Surface plasmons on smooth and rough surfaces and on gratings, *Springer Tracts Mod. Phys.*, 1988, **111**, 1–133.
- 8 M. Nishida, N. Hatakenaka and Y. Kadoya, Multipole surface plasmons in metallic nanohole arrays, *Phys. Rev. B: Condens. Matter Mater. Phys.*, 2015, **91**, 235406.
- 9 S. A. Maier, *Plasmonics: fundamentals and applications*, Springer Berlin, 2007.
- 10 Z. Yong, S. Zhang, C. Gong and S. He, Narrow band perfect absorber for maximum localized magnetic and electric field enhancement and sensing applications, *Sci. Rep.*, 2016, **6**, 24063.
- 11 K. Q. Le, Q. M. Ngo and T. K. Nguyen, Nanostructured metal-insulator-metal metamaterials for refractive index biosensing applications: Design fabrication, and characterization, *IEEE J. Sel. Top. Quantum Electron.*, 2017, **23**, 388–393.
- 12 K. Q. Le, J. Bai, Q. M. Ngo and P. Chen, Fabrication and numerical characterization of infrared metamaterial absorbers for refractometric biosensors, *J. Electron. Mater.*, 2017, **46**, 668–676.
- 13 K. Bhattarai, S. Silva, K. Song, A. Urbas, S. J. Lee, Z. Ku and J. Zhou, Metamaterial perfect absorber analyzed by a meta-cavity mode consisting of multilayer metasurfaces, *Sci. Rep.*, 2017, **7**, 10569.
- 14 Z. Yong, S. Zhang, C. Gong and S. He, Narrow band perfect absorber for maximum localized magnetic and electric field enhancement and sensing applications, *Sci. Rep.*, 2016, **6**, 24063.
- 15 L. X. Li, X. Y. Zong and Y. F. Liu, All-metallic metasurfaces towards high performance magneto-plasmonic sensing devices, *Photonics Res.*, 2020, **8**, 1742–1748.
- 16 T. Maier and H. Bruckl, Wavelength-tunable microbolometers with metamaterial absorbers, *Opt. Lett.*, 2009, **34**, 3012–3014.
- 17 Y. M. Wu, F. Tang, J. Chen, S. H. Shang, J. J. Wu, S. J. Chen, Y. Chen, X. Ye and L. M. Yang, Design of high-efficiency all-dielectric polymer meta-surfaces beam deflection blazed grating, *Results Phys.*, 2020, **17**, 103094.
- 18 H. Singh, B. S. Sohi and A. Gupta, Designing and analysis of cross-shaped CRLH metamaterial for wide band negative index characteristics, *Mater. Res. Express*, 2019, **6**, 075801.
- 19 N. Liu, M. Mesch, T. Weiss, M. Hentschel and H. Giessen, Infrared perfect absorber and its application as plasmonic sensor, *Nano Lett.*, 2010, **10**, 2342–2348.
- 20 X. Chen, W. Li, Z. Wu, Z. Zhang and Y. Zou, Origami-based microwave absorber with a reconfigurable bandwidth, *Opt. Lett.*, 2021, **46**, 1349–1352.
- 21 J. W. Rao, Y. T. Zhao, Y. S. Gui, X. L. Fan, D. S. Xue and C. M. Hu, Controlling Microwaves in Non-Hermitian Metamaterials, *Phys. Rev. Appl.*, 2021, **15**, L021003.
- 22 Z. P. Zheng, Y. Luo, H. Yang, Z. Yi, J. G. Zhang, Q. J. Song, W. X. Yang, C. Liu, X. W. Wu and P. H. Wu, Thermal tuning of terahertz metamaterial properties based on phase change material vanadium dioxide, *Phys. Chem. Chem. Phys.*, 2022, **24**, 8846–8853.
- 23 C. Du, D. Zhou, H. H. Guo, Y. Q. Pang, H. Y. Shi, W. F. Liu, J. Z. Su, C. Singh, S. Trukhanov, A. Trukhanov, L. Panina and Z. Xu, An ultra-broadband terahertz metamaterial coherent absorber using multilayer electric ring resonator structures based on anti-reflection coating, *Nanoscale*, 2020, **12**, 9769–9775.
- 24 X. Cheng, R. Huang, J. Xu and X. Xu, Broadband Terahertz Near-Perfect Absorbers, *ACS Appl. Mater. Interfaces*, 2020, **12**, 33352–33360.
- 25 S. Karmakar, D. Kumar, R. K. Varshney and D. R. Chowdhury, Strong Terahertz Matter Interaction Induced Ultrasensitive Sensing in Fano Cavity based Stacked Metamaterials, *J. Phys. D: Appl. Phys.*, 2020, **53**, 415101.
- 26 R. L. Paldi, X. Sun, X. Wang, X. Zhang and H. Wang, Strain-Driven In-plane Ordering in Vertically Aligned ZnO-Au Nanocomposites with Highly Correlated Metamaterial Properties, *ACS Omega*, 2020, **5**, 2234–2241.
- 27 A. Krishna, J. M. Kim, J. Leem, M. C. Wang, S. Nam and J. Lee, Ultraviolet to Mid-Infrared Emissivity Control by Mechanically Reconfigurable Graphene, *Nano Lett.*, 2019, **19**, 5086–5092.
- 28 N. Lee, T. Kim, J. S. Lim, I. Chang and H. H. Cho, Metamaterial-Selective Emitter for Maximizing Infrared Camouflage Performance with Energy Dissipation, *ACS Appl. Mater. Interfaces*, 2019, **11**, 21250–21257.
- 29 Z. K. Zhou, Y. Chen, Y. H. Tian, J. Liang and W. X. Yang, Ultra-broadband metamaterial perfect solar absorber with polarization-independent and large incident angle-insensitive, *Opt. Laser Technol.*, 2022, **156**, 108591.
- 30 C. F. Guo, T. Y. Sun, F. Cao, Q. Liu and Z. F. Ren, Metallic nanostructures for light trapping in energy-harvesting devices, *Light: Sci. Appl.*, 2014, **3**, e161.
- 31 W. Li and J. Valentine, Metamaterial perfect absorber based hot electron photodetection, *Nano Lett.*, 2014, **14**, 3510–3514.
- 32 Y. Wang, G. Zhu, M. Li, H. Singh, C. Marques, R. Min, B. K. Kaushik, B. Y. Zhang, R. Jha and S. Kumar, Water Pollutants p-Cresol Detection Based on Au-ZnO Nanoparticles Modified Tapered Optical Fiber, *IEEE Trans. Nanobiosci.*, 2021, **20**, 377–384.
- 33 H. Singh, A. Gupta, R. S. Kaler, S. Singh and A. S. Gill, Designing and Analysis of Ultrathin Metamaterial Absorber



- for W Band Biomedical Sensing Application, *IEEE Sens. J.*, 2022, **22**, 10524–10531.
- 34 S. Hong, Y. J. Lee, K. Moon and S. H. Kwon, Double Resonance Perfect Absorption in a Dielectric Nanoparticle Array, *Curr. Opt. Photonics*, 2017, **1**, 228–232.
 - 35 B. L. Zhang, Z. X. Li, Z. D. Hu, J. J. Zhang and J. C. Wang, Analysis of a bidirectional metamaterial perfect absorber with band-switchability for multifunctional optical applications, *Results Phys.*, 2022, **34**, 105313.
 - 36 E. D. Palik, *Handbook of Optical Constants of Solids*, Academic press, 1985.
 - 37 H. Luo, Q. Y. Shangguan, Y. T. Yi, S. B. Cheng, Y. G. Yi and Z. Z. Li, A tunable “Ancient Coin”-type perfect absorber with high refractive index sensitivity and good angular polarization tolerance, *Coatings*, 2021, **11**, 814.
 - 38 J. Yu, J. Zhu, S. Ye and X. Wang, Ultra-wide sensing range plasmonic refractive index sensor based on a two-dimensional circular-hole grating engraved on a gold film, *Results Phys.*, 2021, **26**, 104396.
 - 39 W. L. Barnes, A. Dereux and T. W. Ebbesen, Surface plasmon subwavelength optics, *Nature*, 2003, **424**, 824–830.
 - 40 N. Gupta and A. Dhawan, Bridged-bowtie and cross bridged-bowtie nanohole arrays as SERS substrates with hotspot tunability and multi-wavelength SERS response, *Opt. Express*, 2018, **26**, 17899.
 - 41 K. J. Russella and L. Evelyn, Gap-mode Plasmonic Nanocavity, *Appl. Phys. Lett.*, 2010, **97**, 163115.
 - 42 Z. Q. Wu, J. L. Yang, N. K. Manjunath, Y. J. Zhang, S. R. Feng, Y. H. Lu, J. H. Wu, W. W. Zhao, C. Y. Qiu, J. F. Li and S. S. Lin, Gap-Mode Surface-Plasmon-Enhanced Photoluminescence and Photoresponse of MoS₂, *Adv. Mater.*, 2018, **30**, 1706527.
 - 43 J. Xu, Z. Zhao, H. Yu, L. Yang, P. Gou, J. Cao, Y. Zou, J. Qian, T. Shi, Q. Ren and Z. An, Design of triple-band metamaterial absorbers with refractive index sensitivity at infrared frequencies, *Opt. Express*, 2016, **24**, 25742–25751.
 - 44 J.-Y. Jung, J. Lee, J.-H. Choi, D.-G. Choi and J.-H. Jeong, Enhancement of refractive index sensing for an infrared plasmonic metamaterial absorber with a nanogap, *Opt. Express*, 2021, **29**, 22796–22804.
 - 45 Y. F. C. Chau, C. K. Wang, L. Shen, C. M. Lim, H. P. Chiang, C. T. C. Chao, H. J. Huang, C. T. Lin, N. T. R. N. Kumara and N. Y. Voo, Simultaneous realization of high sensing sensitivity and tunability in plasmonic nanostructures arrays, *Sci. Rep.*, 2017, **7**, 16817.
 - 46 Z. Y. Wang, Y. P. Xu, F. Chen, S. B. Cheng, Z. Yi, G. H. Xiao, Y. H. Li, J. B. Jiang, X. W. Zhou and Z. Y. Chen, Tunable multi-narrowband perfect absorber based on graphene and black phosphorus metamaterial, *Optik*, 2022, **270**, 169932.
 - 47 H. Singh, B. S. Sohil and A. Gupta, Designing and analysis of cross-shaped CRLH metamaterial for wide band negative index characteristics, *Mater. Res. Express*, 2019, **6**, 075801.

